Journal of Southeast University (English Edition) Vol. 42, No. 2, pp. 206-215 June 2026 ISSN 1003-7985

LES of geometric eccentricity effects on flow field and aerodynamic forces of T-shaped towers

ZHAO Shuang[1,2], ZHANG Xianhong[1], ZHANG Chengtao[1], YAN Zhitao[1,2]

(1. School of Civil Engineering and Architecture, Chongqing University of Science and Technology, Chongqing 401331, China; 2. Chongqing Construction Science Research Institute Co., Ltd., Chongqing 400016, China)

Abstract: To investigate the aerodynamic performance of geometrically eccentric structures, wind tunnel testing and numerical simulations were employed to examine the flow field characteristics and tri-component aerodynamic forces of T-shaped towers with varying geometric eccentricities. A mathematical model for their generalized force spectra was established. The reliability of the numerical simulation method was validated by comparing the lift, drag, and torque coefficients obtained from wind tunnel experiments with the numerical results. Subsequently, the influence of geometric eccentricity on wind pressure distribution, vortex shedding characteristics, and turbulent kinetic energy distribution was analyzed. Using random vibration theory, a normalized formula for the full-tower force spectrum of the T-shaped tower was derived through nonlinear fitting of numerical simulation data. The results indicate that with increasing eccentricity, the vortex shedding of the structure becomes more complex, with a bias toward the eccentric side. Its wake morphology undergoes distortion and deformation, exhibiting vertical extensibility and leading to peak wind pressure occurring at the longer cross-arm. Furthermore, the torque coefficient demonstrated the highest sensitivity to eccentricity variations. A 50% increase in eccentricity resulted in a 99.7% increase in the torque coefficient.

Key words: geometric eccentricity; T-shaped towers; aerodynamic forces; flow field characteristics

DOI: 10.3969/j.issn.1003-7985.2026.02.007

In recent years, the rapid expansion of engineering construction has led to the widespread implementation of geometrically eccentric high-rise structures. However, geometric eccentricity significantly alters their aerodynamic characteristics, resulting in enhanced susceptibility to wind load effects in both crosswind and torsional directions[1]. Studies have demonstrated that flow pattern alterations in wake regions may trigger nonlinear coupling effects between torsional moments and crosswind loads[2]. Although the existing literature[3-5] has examined the aerodynamic characteristics of geometrically symmetric structures under independent multidirectional wind loads, systematic methods for evaluating the geometric eccentricity effect under three-dimensional wind direction coupling remain limited. Such evaluation is crucial for the wind-resistant design of geometrically eccentric structures.

Wind tunnel testing and numerical simulation are principal methodologies for investigating structural aerodynamic performance, precisely capturing the dynamic coupling mechanisms of fluid-structure interaction[6-7]. Aeroelastic models achieve consistency in dynamic responses between prototypes and scaled models by maintaining geometric and dynamic similarity. During testing, the dynamic responses of scaled models are directly measured, and dimensional analysis principles are subsequently applied to extrapolate prototype response characteristics from experimental data[8]. With current advances in computational power, numerical simulation methods have gradually become prevalent because of their significant cost advantages and multiphysical field analysis capabilities[7]. Among these methods, large eddy simulation (LES) can directly resolve large-scale vortices and retain unsteady flow pulsation characteristics, making it a powerful and widely used tool in the field[9-11].

Accurate assessment of the wind-induced vibration of geometrically eccentric structures requires a thorough understanding of their aerodynamic and wind load characteristics. Previous research on structural aerodynamic performance has predominantly focused on structures without geometric eccentricity[3-4,9]. However, T-shaped aerodynamically eccentric structures, such as tower cranes, eccentric billboards, support structures, and eccentric transmission towers, are prevalent in practical engineering[12]. The T-shaped tubular tower studied herein consists of two cylinders, and its flow separation locations and patterns differ significantly from those of a single cylinder.

Aerodynamic shape significantly influences the aerody-

Received 2025-06-05, **Revised** 2025-10-15.

Biographies: ZHAO Shuang (1989—), male, doctor, lecturer; YAN Zhitao (corresponding author), male, doctor, professor, yanzhitao@cqu.edu.cn.

Foundation items: The China Postdoctoral Science Foundation (No. 2023T160767), the Natural Science Foundation of Chongqing Municipality (No. CSTB2023NSCQ-MSX0751).

Citation: ZHAO Shuang, ZHANG Xianhong, ZHANG Chengtao, et al. LES of geometric eccentricity effects on flow field and aerodynamic forces of T-shaped towers[J]. Journal of Southeast University (English Edition), 2026, 42(2): 206-215. DOI: 10.3969/j.issn.1003-7985.2026.02.007.

namic performance of structures[13]. Therefore, when a structure is aerodynamically eccentric, its aerodynamic performance markedly differs from that of a noneccentric structure. Previously, a series of wind tunnel tests on symmetric T-shaped towers revealed that the cross-arm is significantly affected by crosswind[14]. Structures with aerodynamically eccentric shapes may experience greater wind effects in the crosswind direction and torsional moment than non-eccentric structures, necessitating further investigation. In addition, current codes or standards[15-16] lack explicit guidelines for assessing wind effects on eccentric structures.

In terms of structural wind load calculation, existing research primarily establishes empirical formulas for crosswind aerodynamic forces on rectangular structures based on experiments[17], verifies the reliability of crosswind power spectra using first-mode generalized force spectra[18], and proposes simplified expressions for torsional generalized wind loads[19]. However, traditional approaches have shown limitations in accurately estimating wind effects on irregular geometries. Thus, boundary layer wind tunnel tests have been conducted to develop empirical formulas for crosswind dynamic loads and wind-induced torque on L-shaped structures[20]. Nevertheless, previous studies on the aerodynamic eccentricity effects of structures have mainly concentrated on a limited number of specific eccentric conditions. Given the significant influence of aerodynamic shape on structural aerodynamic performance, previous findings may not be directly applicable to T-shaped towers. Furthermore, the tri-component aerodynamic forces of geometrically eccentric T-shaped structures remain inadequately explored, highlighting the need for a unified computational framework considering the coupled effects of alongwind, crosswind, and torsional loads.

Based on the above review, this study integrates numerical simulation and wind tunnel testing to investigate the aerodynamic performance of geometrically eccentric structures. A computational framework is proposed for wind loads on T-shaped towers under three-dimensional coupled wind actions with varying geometric eccentricities.

1 Numerical Simulation

1.1 Geometric modeling and grid scheme

The calculation accuracy of fluid mechanics mainly depends on the size of the calculation domain and the choice of grid mode. In this study, the tower's main body is a cylindrical structure, so the wind flow is characterized by bluff-body aerodynamics around it. By controlling the blockage rate of the basin, model position, and the thickness of the wall mesh, the calculation domain grid of the flow around the tower is determined. Excessive blockage can adversely affect the flow field turbulence on the side of the cylinder and the wind pressure on the surface of the cylinder, resulting in inaccurate calculation results. Accordingly, the computational domain size, mesh strategy, and other settings are determined according to Ref. [21].

As illustrated in Fig. 1(a), the calculation domain covers the ranges of $20H$ in the streamwise direction, $6H$ in the crosswind direction, and $6H$ in the vertical direction. Notably, the left and right surfaces serve as symmetrical boundary conditions, where the height of the vertical rod H=0.45 m. Table 1 presents the geometric parameters of eccentricity. M1 to M6 represent six eccentricity models with different sizes. The transverse rod radius r_t and the vertical rod radius r_v are 3 and 15 mm, respectively. The key analytical parameter, eccentricity ($e = L_t'/L_t$), is defined as the ratio of the long side of the transverse rod L_t' to the full length of the transverse rod L_t. The blockage rate is 0.31% under this arrangement. The eccentric T-shaped cylindrical tube tower model is segmented to determine the correlation of the local

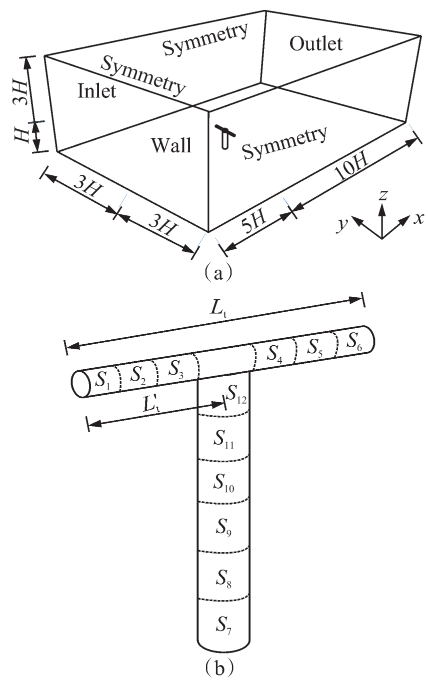

Fig. 1 Calculation of domain boundary conditions and model segmentation. (a) Calculation of basin size and boundary conditions; (b) T-tower model

Table 1 Geometric parameters

Model No.	e	L_t/mm	L_t'/mm
M1	0.50	180	90
M2	0.55	180	99
M3	0.60	180	108
M4	0.65	180	117
M5	0.70	180	126
M6	0.75	180	135

tri-component forces of the tower. As illustrated in Fig. 1 (b), both the transverse and vertical rods are divided into six equal segments, designated as S1 to S6 and S7 to S12, respectively.

LES directly resolves large-scale vortices and retains unsteady flow pulsation characteristics, making it suitable for turbulence modeling in this paper. This study investigates the influence mechanisms of aerodynamic eccentricity on flow-field characteristics using a uniform flow field as the inflow condition. The average wind speed at the inlet is set to 4 m/s, and the Reynolds number Re=3 300. The watershed grid is discretized using a hybrid grid division scheme with inner and outer domains: the inner domain near the wall of the tower model adopts an unstructured grid to adapt to the local irregular surface of the tower, whereas the outer domain far away from the model adopts a structured grid. The interface boundary conditions provided by FLUENT 19. 2 are used for data exchange between the structured and unstructured grids. As the boundary layer surrounds the model, the height of the first element and the dimensionless wall distance are set to $0.003r_t$. The near-wall y^+ value is about 35-85, which is suitable for LES wall function. The internal tetrahedral grid growth ratio is 1. 1, and the total grid number reaches 6×10^6, meeting acceptable accuracy and computational cost. Computational grid schemes around the tower are shown in Fig. 2.

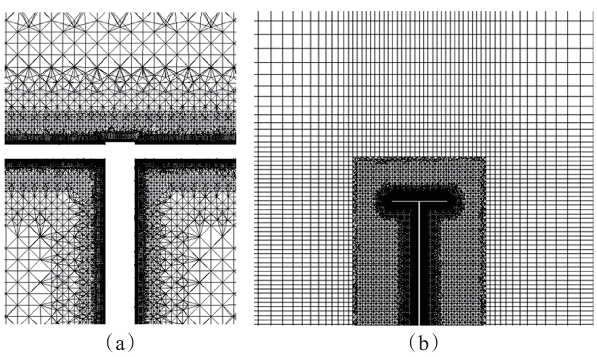

Fig. 2 Computational grid schemes around the tower. (a) Boundary layer view; (b) Global area view

1. 2 Simulation settings

For the governing equations pertinent to numerical discretization and solution, such as the continuity equation, momentum equations, and the LES filtering function, readers are referred to are detailed in Ref. [22] and are not repeated here. The pressure implicit with the splitting of operators algorithm was used for numerical simulation. Temporal discretization used the implicit second-order format, whereas space discretization adopted a second-order center format. Because LES is suited for high-Reynolds-number flows, the wall-adapting local eddy-viscosity subgrid-scale model was used to analyze low-Reynolds-number flows near the wall. To meet the high-performance requirement of LES, 18-core parallel computing was adopted. According to Ref. [23], the numerical stability of the Courant number is generally good when it ranges from 0 to 5, and the calculation time is reduced. To satisfy the Courant-Friedrichs-Lewy condition, the time step in this paper was set as Δt=0. 3 ms.

1. 3 Data processing

In this study, nondimensional data coefficients are employed to discuss the results for simplicity and effectiveness. The pressure coefficient is given as follows:

$$C_p = \frac{P - P_0}{0.5\rho U_H^2} \tag{1}$$

where P and P_0 represent the static pressure of the structure surface and the reference pressure (0 Pa), respectively; ρ is the air density; and U_H is the wind speed at the height of the tower vertex position (reference position).

The tri-component aerodynamic force coefficients are described as

$$C_{Fni} = \begin{cases} \dfrac{\bar{F}_{S_n i}}{0.5\rho U_{HS_n}^2 A_{S_n}} & i = 1, 2 \\ \dfrac{\bar{F}_{S_n i}}{0.5\rho U_{HS_n}^2 A_{S_n} L_t} & i = 3 \end{cases} \tag{2}$$

where i=1, 2, 3 represent the model drag, lift, and torque, respectively. The model segment number is denoted by S_n, where n=1, 2, ⋯, 12, as shown in Fig. 1 (b); A_{S_n} is the windward area of section S_n of the model, $\bar{F}_{S_n i}$ is the mean tri-component aerodynamic force of section S_n; and U_{HS_n} is the wind speed at the height of the geometric center of section S_n.

The correlation coefficient is described as

$$\mathrm{Cor}(m, r) = \frac{\mathrm{Cov}(m, r)}{\sigma_m \sigma_r} = \frac{\sum(\theta_m - \bar{\theta}_m)(\theta_r - \bar{\theta}_r)}{\sqrt{\sum(\theta_m - \bar{\theta}_m)^2 \sum(\theta_r - \bar{\theta}_r)^2}} \tag{3}$$

where Cov(m, r) is the covariance of variables m and r; σ_m and σ_r represent the standard deviation of m and r, respectively; θ represents the time velocity history in the X, Y, or Z direction. The upper line represents the time average of the variables.

1. 4 Results validated through wind tunnel testing

A high-frequency force balance (HFFB) test was conducted on the standard T-shaped tube tower model (M1) in the wind tunnel laboratory of the Tianjin Academy of Water Sciences, as shown in Fig. 3. Ref. [24] detailed the wind tunnel test procedures and model fabrication. A high-frequency six-component torque sensor was used to measure the model's downwind drag, crosswind lift, and torque time history around the central axis. The wind-vibration response of the tower was calculated according to the random vibration theory by combining the tri-component aerodynamic force time history data of the T-shaped tower with the structure's dynamic characteristics. The sampling frequency and duration were set to 1 000 Hz and 60 s, respectively. The wind tunnel test chamber and T-shaped tower model of the HFFB test are shown in Fig. 3(b). M1, M3, and M6 had dimensions similar to those used in the numerical simulation. The test wind field had uniform flow, and the wind speed at the top 0.45 m of the T-shaped tower model was 4.0 m/s.

(a)

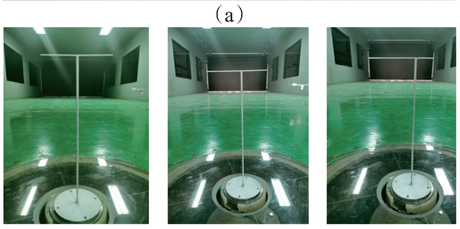

M1 M3 M6

(b)

Fig. 3 Photos of HFFB test. (a) TK-400 DC wind tunnel laboratory; (b) T-shaped tower rigidity models

To verify the accuracy of the numerical simulation, the same model parameters and wind field parameters were adopted as in the wind tunnel test. The three components of the aerodynamic force were selected as the error evaluation metric. The base tri-component aerodynamic force measured by a force balance installed beneath the T-shaped structure during wind tunnel tests was compared with that obtained from numerical simulations.

The relative errors of the tri-component aerodynamic force of the entire tower model are summarized in Table 2. The overall tri-component aerodynamic force coefficient from the numerical calculation shows acceptable consistency with the experimental results. There are certain gaps between the lift and torque coefficients, primarily due to the complex flow conditions on the side and lee sides. Despite these differences, the maximum relative error of individual points is still less than 10%. Huang et al. [25] also reported a similar phenomenon, with the drag coefficient having a relatively better fitness. The error (E) is defined as $E = (S_v - W_v)/W_v \times 100\%$, where S_v represents the numerical simulation value and W_v denotes the wind tunnel test value. In addition, the drag coefficient power spectral density (PSD) from wind tunnel tests and numerical simulations shows good agreement in major frequency components, peak locations, and energy distribution, particularly in the mid-to-low frequency range. The consistent energy decay in high frequencies further confirms the model's capability in capturing flow dynamics and validates its reliability, as shown in Fig. 4.

Table 2 Relative errors of overall tri-component aerodynamic force obtained through numerical simulations and wind tunnel tests

Model No.	Relative error/%		
	Drag	Lift	Torque
M1	2.64	8.88	3.26
M2	1.64	7.62	8.45
M3	3.82	6.61	7.49

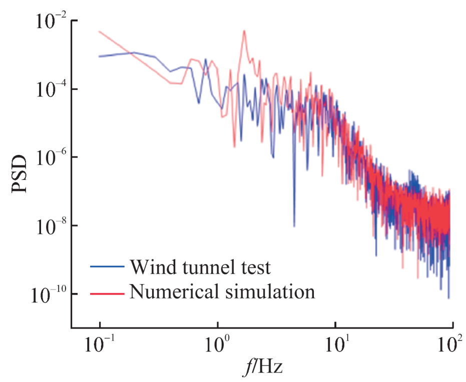

Fig. 4 Comparison of drag coefficient PSD for Model M4

2 Results and Discussion

2.1 Tri-component aerodynamic force coefficient and wind pressure distribution

Table 3 compares the drag, lift, and torque coefficients of the whole tower with different eccentricities. The aerodynamic eccentricity significantly affected the torque coefficient, which was caused by the imbalance of the instantaneous wind pressure distribution on the tower surface due to the structural eccentricity. In addition, larger eccentricities led to greater increases in tower torque. Specifically, when the eccentricity increased from 0.50 to 0.55, the mean value of the overall torque coefficient of the tower increased by 0.007 8. When the eccentricity increased from 0.70 to 0.75, the mean torque coefficient of the overall tower increased by 0.010 7. When the wind flow passed the tower's edge, the tower surface blocked it, thus changing the speed and direction of the wind flow, which ultimately led to transverse lift and torsional torque. Meanwhile, as the eccentricity increased by 50%, the mean torque increased by 99.7%. The mean lift force showed a fluctuating trend, and the mean lift coefficients were equal when the eccentricities were 0.50 and 0.75. The fluctuating components of the overall lift and torque of the tower increased by 16. 32% and 99. 50%, respectively. For the drag coefficient, when the eccentricity increased by 50%, the maximum change rate of the mean drag coefficient was 0. 18%, and the maximum change rate of the drag fluctuating component was 0. 20%. In summary, increases in eccentricity affect the mean and fluctuating components of lift and torque, which have a significant impact on torque but have less effect on drag.

Table 3 Changes in overall tri-component aerodynamic force under different eccentricities

Eccentricity	Overall drag coefficient		Overall lift coefficient		Overall torque coefficient	
	Mean	RMS	Mean	RMS	Mean	RMS
0.50	0.846 3	0.846 4	0.000 9	0.004 1	0.000 1	0.000 2
0.55	0.845 3	0.845 5	0.001 0	0.004 3	0.007 9	0.008 1
0.60	0.846 3	0.846 5	0.000 6	0.004 5	0.015 9	0.016 1
0.65	0.846 9	0.847 2	0.001 6	0.004 6	0.023 8	0.024 4
0.70	0.846 9	0.847 0	0.001 7	0.004 6	0.029 1	0.029 9
0.75	0.846 1	0.846 2	0.000 9	0.004 9	0.039 8	0.040 2

This paper presents the continuous-time history values of the three components of the overall aerodynamic force obtained through numerical simulation. The absolute values of the correlation coefficients for these aerodynamic force components, derived using Eq. (3), varied with eccentricity, as illustrated in Fig. 5. The correlation between drag, lift, and torque increased roughly with the increase in eccentricity; the correlation between drag and lift experienced a sharp change at an eccentricity of 0. 60 but had an overall acceleration trend. As the eccentricity increased, the changes in the correlation between drag and torque and between lift and torque were accelerated, which could be attributed to the increase in the variation amplitude of the torque coefficient mentioned above under high eccentricity.

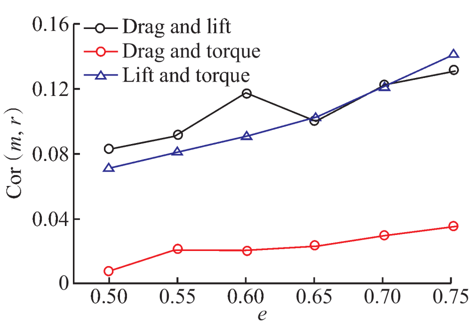

Fig. 5 Correlation of three components of overall aerodynamic force with eccentricity

The mean pressure distribution on the windward side of the structure under different eccentricities is shown in Fig. 6. Notably, the stagnation point of the windward side was located at the model height of 0. 967H, which was basically on the same horizontal line as the central axis of the cross-arm. Meanwhile, because of eccentricity, the symmetry of the windward pressure distribution on the vertical rod was altered. In addition, as the eccentricity increased, the wind pressure at the right end of the transverse rod intensified and became more concentrated. This could generate a large local wind pressure on the surface of the eccentric structure for general structures, resulting in greater structural wind-induced vibration response.

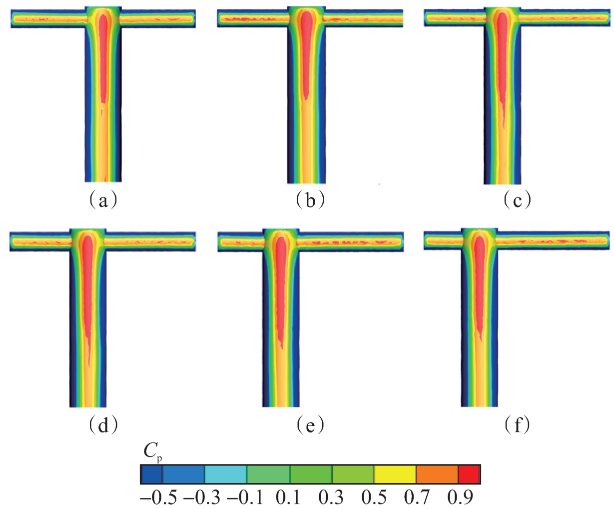

Fig. 6 Pressure distribution on windward side of tower under different eccentricities. (a) M1; (b) M2; (c) M3; (d) M4; (e) M5; (f) M6

Aerodynamic eccentricity also influenced the pressure distribution on the leeward surface of the model, as shown in Fig. 7. Specifically, compared with model M1, the suction effect in the height range of about 3/4H to H at the upper end of the vertical rod of the other models increased, resulting in greater pressure on the leeward surface. For example, as the eccentricity rose by 30%, the peak pressure coefficient of model M4 increased by

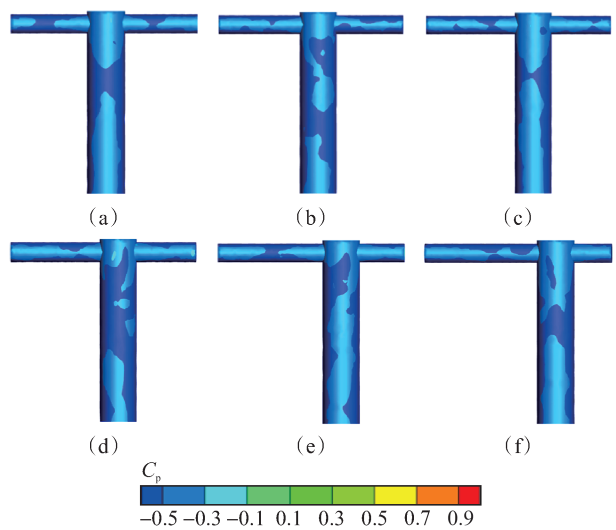

Fig. 7 Pressure distribution on leeward side of tower under different eccentricities. (a) M1; (b) M2; (c) M3; (d) M4; (e) M5; (f) M6

7.5%. In addition, an increase in eccentricity from 0.50 (without eccentricity) to 0.65 significantly changed the distribution of local pressure regions on the leeward surface. The symmetrical distribution of model M1 gradually became disordered, potentially causing wind pressure differences that may affect the aerodynamic distribution of the structure.

2.2 Flow field and vortex structure

To explain the aerodynamic variation under different eccentricities, the flow field and vortex structure were further observed. This study focused on three models: M1, M4, and M6. Time-averaged velocity contours with streamlines on horizontal planes at different heights were compared for M1, M4, and M6, as shown in Fig. 8.

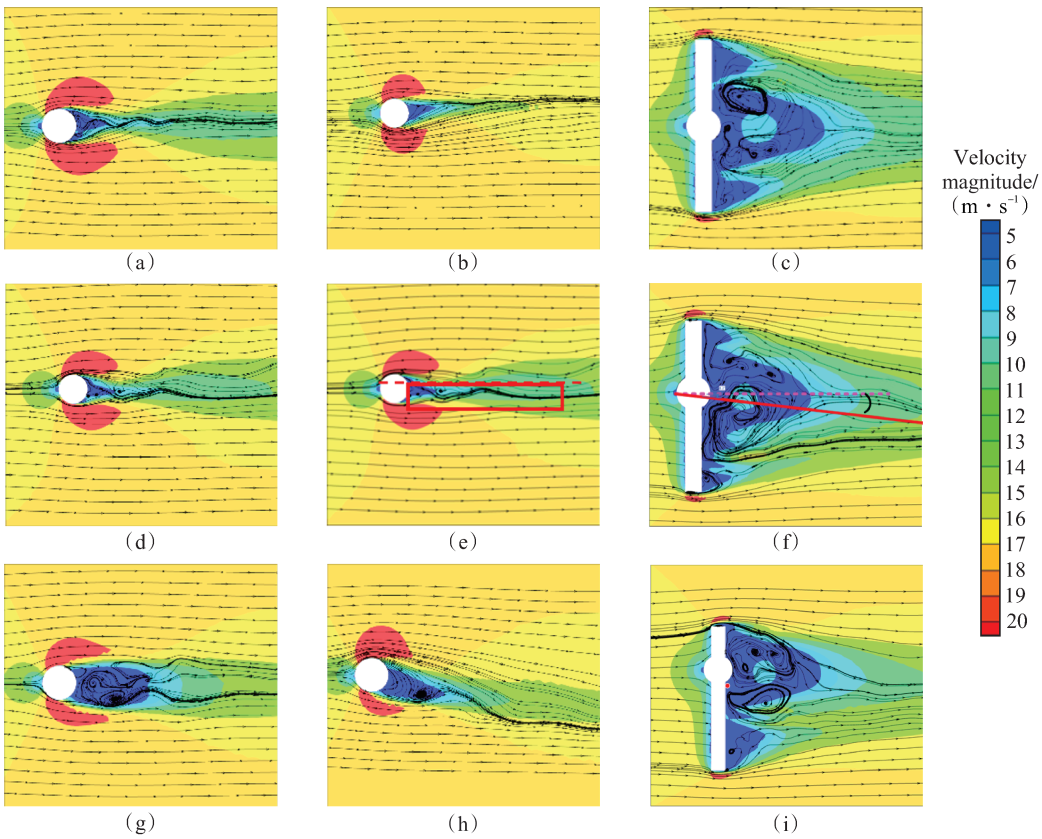

Fig. 8 Contours of mean velocity on the horizontal planes at different heights with time-averaged streamlines for M1, M4, and M6. (a) M1, z=0.15 m; (b) M1, z=0.25 m; (c) M1, z=0.29 m; (d) M4, z=0.15 m; (e) M4, z=0.25 m; (f) M4, z=0.29 m; (g) M6, z=0.15 m; (h) M6, z=0.25 m; (i) M6, z=0.29 m

It is evident that the eccentricity significantly modifies the flow streamlines and vortex structure around the tower. Specifically, for M1 (Figs. 8(a)-(c), the shear layer evenly separated the structure's left and right sides at all heights, which thus generated symmetric vortex shedding along the streamwise direction. However, M1, M4, and M6 showed distinctive flow separation and reattachment degrees and phase motion appearing in horizontal planes at different heights. The asymmetric recirculation area tended to incline toward the long arm of the transverse rod and extend downstream, which changed the wind speed and direction of the flow field and directly increased the negative pressure on the leeward surface of the upper end of the eccentric vertical rod. In addition, although the windward surface did not change much, the stagnation points on the leeward surface (see the red point in Fig. 8(i)) shifted with eccentricity, which led to an overall enhancement of the tower's torque. The separation bubbles under M4 were no longer symmetrical, as indicated by the red box in Fig. 8(e). In contrast, the separate shear layer in the short-arm direction of the cross-arm was flatter and was immersed in the deviated wake flow. This variation in bubble attachment position can fully explain the wind pressure distribution: the more bubbles are attached, the greater the wind pressure is. This can also describe the sudden change in the mean and RMS pressure coefficients on the leeward surfaces.

The Q-criterion was used to visualize the pressure-colored vortex structure to further compare the instantaneous flow feature and analyze the changes in turbulent kinetic energy. As shown in Fig. 9, the flow region close to the structure, influenced by eccentricity, was characterized by nonuniformity, small-scale fragments, downstream deflection, and distortion. These different flow-structure interactions were the underlying mechanisms that generated irregular wind pressure distributions and asymmetrical aerodynamics. The conical vortex structure at the upper end of the vertical rod was enhanced because of the asymmetric vortex on both sides of the transverse rod, as shown by black ovals in Fig. 9. This enhanced vortex structure led to changes in wind pressure at the upper end of the tower's leeward surface. The large-scale vortex structures were broken into small eddies, especially in the wake region near the vertical rod (see blue ovals). The vortex in the direction of the cross-arm not only extended downstream to far wakes but also deflected toward the right side, which was also the direction of the torque force (see black ovals in Fig. 9(f)).

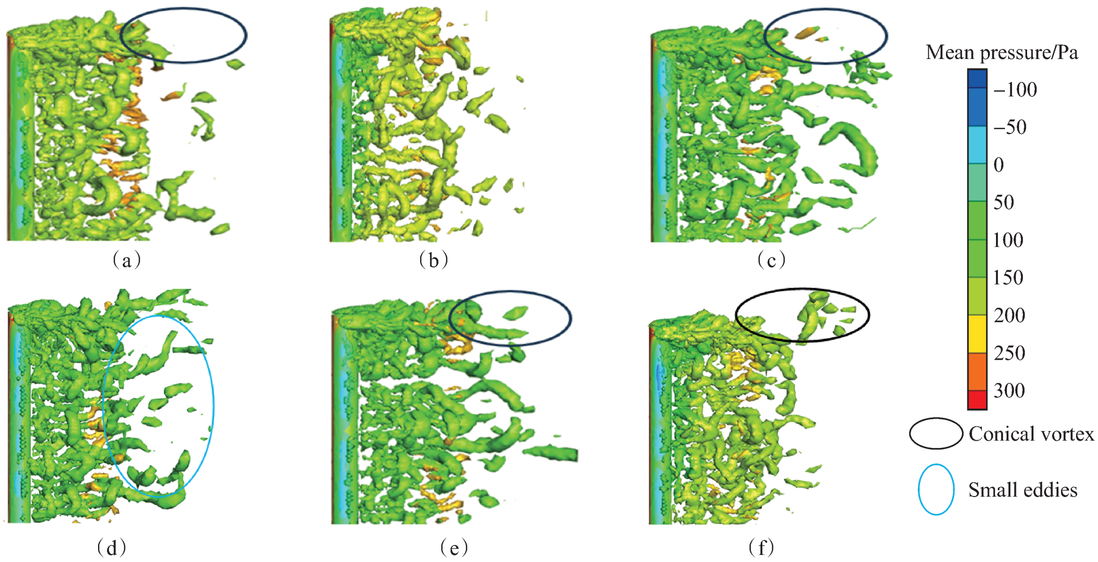

Fig. 9 Time evolution of vertical instantaneous vortex structures. (a) M1; (b) M2; (c) M3; (d) M4; (e) M5; (f) M6

3 Mathematical Model of Aerodynamic Loads for T-Shaped Tower

According to the random vibration theory, the cross-PSD of the tri-component aerodynamic force S_{Fij} on different heights can be calculated using the following expressions:

$$S_{Fij}(x_1, x_2; f) = C_{FS_n ij}(x_1) C_{FS_n ij}(x_2) S'_{Fi}(f) \mathrm{Cor}_{Fij}(x_1, x_2) \quad (4)$$

$$S'_{Fi}(f) = \frac{S_{Fi}(f)}{\sigma_{Fi}^2} \quad (5)$$

where j=1, 2 represent the vertical direction (vertical rod extension direction) and transverse direction (transverse rod extension direction), respectively; x_1 and x_2 are the coordinates of two points in the space of the tower's vertical or horizontal bar; f is the frequency; $S'_{Fi}(f)$ represents the nondimensionless tri-component aerodynamic force spectrum of the overall tower; $C_{FS_n ij}$ is the aerodynamic coefficient; $\mathrm{Cor}_{Fij}(x_1, x_2)$ is the transverse or vertical correlation coefficient of the tri-component aerodynamic force coefficient, which is due to the mainly vertical extension of the T-shaped tower model; and σ_{Fi} is the RMS of aerodynamic force. $S'_{Fi}(f)$, $C_{FS_n ij}$, and $\mathrm{Cor}_{Fij}(x_1, x_2)$ are three key factors in determining the cross-spectral density of the tri-component aerodynamic force in Eq. (4). Because it is difficult or even impossible to derive the analytical expression of Eq. (5), numerical simulation is typically used. In this study, the nonlinear least-squares method (NLSM) was adopted, and the calculation of Eq. (5) was established on the basis of the numerical simulation results. The eccentricity e and height z were selected as key variables.

3.1 Overall tri-component aerodynamic force PSD

The overall aerodynamic tri-component force time history of the T-shaped tower model under different eccentricities was analyzed using the fast Fourier transform, and the overall lift and torque power spectrum appearance maintained a wide range of consistency. As the frequency increased, the overall power lift spectrum appearance of the tower in the high-frequency band gradually resembled the overall drag power spectrum. It became gentler, and the amplitude got closer to the high band of the whole drag power spectrum. Therefore, this phenomenon could be associated with the aforementioned tri-component aerodynamic force correlation, which intensified with increasing eccentricity, as illustrated in Fig. 5. Through the nonlinear fitting of the numerical simulation results, the normalized formula of the whole force spectrum of the T-shaped tower is proposed.

$$\frac{fS_{Fi}(f)}{\sigma_{Fi}^2} = \varepsilon_{i1} + \varepsilon_{i2} f^2 + \varepsilon_{i3} f^3 + \varepsilon_{i4} f^4 + \varepsilon_{i5} f^5 \quad (6)$$

$$\varepsilon_{ip} = \chi_p + \delta_p e + \varphi_p e^2 \quad (7)$$

where ε_{ip} is a function of e; χ_p, δ_p, and φ_p are fitting parameters. The fitting parameters for Eq. (7) are presented in Table 4.

Table 4 Determination of parameters ε_{ip}

ε_{ip}	χ_p	δ_p	φ_p
ε_{11}	45.748 17	27.111 89	−69.592 50
ε_{12}	−90.549 30	−25.903 70	99.900 57
ε_{13}	62.203 19	−15.466 40	−31.670 10
ε_{14}	−17.889 50	12.146 69	0.449 43
ε_{15}	1.811 63	−1.868 01	0.657 07
ε_{21}	48.707 03	27.376 79	43.350 99
ε_{22}	−88.840 30	−53.609 50	−82.552 30
ε_{23}	52.356 77	31.481 27	48.957 52
ε_{24}	−13.107 50	−7.904 34	−12.222 80
ε_{25}	1.163 83	0.701 20	1.076 02
ε_{31}	18.086 18	19.089 07	7.969 87
ε_{32}	−44.562 10	−45.660 10	−21.488 80
ε_{33}	29.828 64	26.895 99	14.394 96
ε_{34}	−8.231 89	−6.807 81	−4.132 13
ε_{35}	0.781 99	0.606 52	0.404 45

Table 5 Determination of parameters θ_{ijg}

θ_{ijg}	a_i	b_i	c_i
θ_{111}	1.330 51	−2.209 78	1.713 07
θ_{112}	−1.406 24	3.673 53	−2.638 64
θ_{113}	1.517 79	−4.036 80	2.969 57
θ_{211}	0.948 96	−2.377 88	1.028 43
θ_{212}	2.112 16	−2.782 53	−3.825 82
θ_{213}	−2.033 24	−1.812 22	−0.758 33
θ_{311}	0.078 58	−4.144 84	−2.375 18
θ_{312}	3.010 15	−4.707 8	4.288 54
θ_{313}	2.303 31	−0.113 91	0.785 25
θ_{121}	−2.627 16	−0.411 51	4.630 89
θ_{122}	0.468 06	0.211 36	−2.684 06
θ_{123}	−0.111 02	1.240 60	1.791 36
θ_{221}	−1.044 85	−1.325 63	4.879 82
θ_{222}	−4.622 61	3.851 68	4.132 87
θ_{223}	2.961 84	−4.012 88	−2.381 29
θ_{321}	−1.646 43	1.797 28	−3.634 47
θ_{322}	2.212 27	−3.932 38	1.537 57
θ_{323}	−0.058 26	2.790 52	2.150 37

3.2 Aerodynamic force coefficient

The drag, lift, and torque coefficients of the T-shaped tower were fitted using polynomials, with the relative height z/H, relative width y/B, and e as the independent variables. Here, y and z represent the transverse (Y) and vertical (Z) coordinates of the geometric center of section S_n of the tower, respectively. Then, NLSM was applied to fit the coefficients as functions of eccentricity, yielding the following formulas:

$$C_{Fij}(x_j, e) = \theta_{ij1} + \theta_{ij2}x_j + \theta_{ij3}x_j^2 \quad (8)$$

$$x_j = \begin{cases} z/H & j = 1 \\ y/B & j = 2 \end{cases} \quad (9)$$

$$\theta_{ijg} = a_i + b_i e + c_i e^2 \qquad g = 1, 2, 3 \quad (10)$$

where θ_{ijg}, a_i, b_i, and c_i are fitting parameters. The fitting parameters for Eq. (10) are presented in Table 5.

To validate the aforementioned formula, the discrepancies between the numerical simulation results and the calculated outcomes from Eq. (8) are presented in Fig. 10. The error rates for all parameters are less than 5%, thereby validating the applicability of the proposed formula.

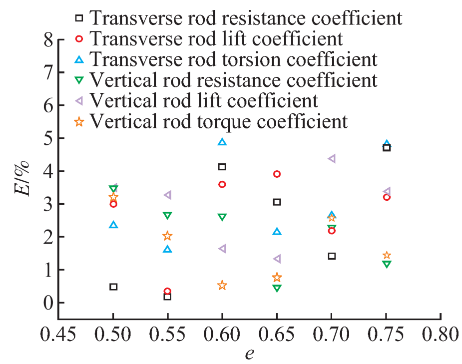

Fig. 10 Errors between numerical simulation and calculation results of Eq. (8)

3.3 Correlation coefficient

The correlation coefficient is defined in Eq. (3). According to the specific attributes of the T-shaped tower model analyzed in this study, the transverse and vertical bars were separately examined. The investigation of the vertical bar primarily focused on vertical correlation, whereas the analysis of the horizontal bar concentrated on horizontal correlation. For the vertical and horizontal bars of the model, the vertical correlation coefficient (the reference point is the top of the vertical bar of the model) and the horizontal correlation coefficient (the reference point is the rightmost end of the horizontal bar of the model) both decreased gradually with the increase in the distance between the two points and finally tended to be flat. New expressions for the vertical and horizontal correlation coefficients are derived from the experimental and numerical simulation results, which depend on the eccentricity through the parameter j:

$$\mathrm{Cor}_{Fij}(x, x) = C_{r1}\exp(-C_{r2}x) \quad (11)$$

$$C_{ru} = A_u + B_u u + C_u e^2 + D_u e^3 \qquad u = 1, 2 \quad (12)$$

where C_{ru} is an eccentricity-dependent coefficient; $x = (x_1 - x_2)/H$; A_u, B_u, C_u, and D_u are fitting parameters. The fitting parameters for Eq. (12) are presented in Tables 6 and 7.

The k-th generalized force spectrum can provide the wind load excitation at different frequencies and accurately establish the mathematical model of the aerodynamic load of a T-shaped tower, which helps predict the behavior and response of the system. Therefore, accord-

Table 6 Relevant parameter values for C_{r1}

F_{ij}	A_1	B_1	C_1	D_1
F_{11}	75.36	−372.23	616.34	−336.24
F_{12}	13.93	−83.91	169.02	−105.71
F_{21}	−129.86	625.32	−980.46	506.98
F_{22}	−25.37	107.30	−141.30	59.42
F_{31}	−58.33	286.90	−465.00	250.64
F_{32}	−132.73	648.28	−1 035.05	546.75

Table 7 Relevant parameter values for C_{r2}

F_{ij}	A_2	B_2	C_2	D_2
F_{11}	−150.89	759.80	−1 211.63	636.44
F_{12}	72.92	−370.28	634.27	−355.55
F_{21}	−7.34	47.26	−62.40	28.60
F_{22}	−123.64	593.83	−927.33	478.08
F_{31}	−37.02	186.01	−300.05	160.67
F_{32}	−148.45	734.05	−1 177.51	622.70

ing to the above nonlinear fitting and random vibration theory, the k-th generalized force spectrum $S^*_{Fki}(f)$ is obtained as follows:

$$S^*_{Fki}(f)=\int_0^H\int_0^H S_{Fij}(x_1,x_2;f)\varphi_k(x_1)\varphi_k(x_2)\mathrm{d}x_1\mathrm{d}x_2 \quad (13)$$

where $\varphi_k(x_1)$ and $\varphi_k(x_2)$ are the k-th modes at the x_1 and x_2 positions, respectively. When Eq. (4) is substituted into Eq. (13) and combined with Eq. (2), the k-th generalized force spectrum is simplified as follows:

$$S^*_{Fki}(f)=\frac{(0.5\rho U_H^2)^2 A_{S_n}(x_1)A_{S_n}(x_2)\bar{F}_{S_n i}{}^2 S_{Fi}(f)}{\sigma^2_{F_i}}\cdot \int_0^H\int_0^H C_{FS_n ij}(x_1)C_{FS_n ij}(x_2)\mathrm{Cor}_{Fij}(x_1,x_2)\cdot \varphi_k(x_1)\varphi_k(x_2)\mathrm{d}x_1\mathrm{d}x_2 \quad (14)$$

where A_{S_n} is the windward area of section S_n of the model; $S_{Fi}(f)$ is the tri-component aerodynamic force spectrum of the overall tower.

4 Conclusions

(1) With increasing geometric eccentricity of the cross-arm in T-shaped towers, lift and torque fluctuations are amplified, whereas drag effects remain minimal. Concurrently, eccentricity redistributes leeward surface pressure, concentrating extreme negative pressure zones on the distal end of the cross-arm relative to the central mast. Aerodynamic eccentricity significantly alters the flow streamline distribution and vortex structures around the tower. The symmetry breaking of leeward separation vortices on the vertical rod complicates vortex-shedding patterns, causing the asymmetric recirculation zone to deviate toward the long-arm side of the cross-arm and extend downstream, directly increasing the overall torque of the tower structure.

(2) Torsional response demonstrates the highest sensitivity to aerodynamic eccentricity: a 50% increase in eccentricity elevates the mean torque by 99.7% and augments torque fluctuations by 99.5%. Increased eccentricity enhances interactions between wakes at different vertical heights, resulting in vertical wake extension. The cross-arm vortices not only extend downstream to the far-wake region but also twist toward the torque direction. This phenomenon further amplifies lateral and torsional responses under aerodynamic eccentricity.

(3) With increasing eccentricity of the T-shaped tower, the low-frequency bands of the tri-component aerodynamic force power spectra exhibit asymptotic attenuation, whereas the high-frequency bands (particularly the full-tower lift spectrum) display amplified fluctuations. Based on the random vibration theory, a normalized full-tower force spectrum formula for the T-shaped tower is established through the nonlinear fitting of the numerical simulation results, facilitating analysis of eccentricity effects on tri-component aerodynamic force characteristics. Moreover, high eccentricity ratios (e=0.70, 0.75) result in greater variation ranges of the full-tower torque, necessitating special attention to structures with high eccentricity in wind-resistant design. Furthermore, in the present numerical simulation, uniform flow is employed as the inlet condition, and boundary layer wind effects are not simulated. Thus, the generalized force spectrum formula must be further refined to account for actual wind effects in future studies.

References

[1] CHEN X Z, KAREEM A. Coupled dynamic analysis and equivalent static wind loads on buildings with three-dimensional modes[J]. Journal of Structural Engineering, 2005, 131(7): 1071-1082.

[2] HOU F W, JAFARI M. Investigation approaches to quantify wind-induced load and response of tall buildings: A review[J]. Sustainable Cities and Society, 2020, 62: 102376.

[3] FU X, LI H N, LI G, et al. Advances in calculation theory of wind and rain loads and failure estimation for transmission tower-line systems[J]. Journal of Building Structures, 2023, 44(3): 198-212. (in Chinese)

[4] LIU Y D, LIN Y X, CHEN Y, et al. Wind-induced response analysis of transmission tower based on a novel analytical tornado model[J]. Journal of Southeast University (Natural Science Edition), 2025, 55(1): 124-130. (in Chinese)

[5] LIN Z Y, LI M, ZHANG H C, et al. Influence of wind barriers on aerodynamic forces of vehicles on bridge decks at different wind attack angles[J]. Journal of Southeast University (Natural Science Edition), 2025, 55(1): 154-160. (in Chinese)

[6] LI J K, MA C M, WU B, et al. Experimental investigation in nonlinear aerodynamic characteristics of a

double-layer truss girder[J]. Journal of Fluids and Structures, 2025, 134: 104284.
[7] BAI H M, WANG N N, WAN D C. Numerical study of aerodynamic performance of horizontal axis dual-rotor wind turbine under atmospheric boundary layers[J]. Ocean Engineering, 2023, 280: 114944.
[8] MA T T, ZHAO L, SHEN X M, et al. Case study of three-dimensional aeroelastic effect on critical flutter wind speed of long-span bridges[J]. Journal of Wind Engineering and Industrial Aerodynamics, 2021, 212: 104614.
[9] WANG Y, CHEN X Z. Evaluation of wind loads on high-rise buildings at various angles of attack by wall-modeled large-eddy simulation[J]. Journal of Wind Engineering and Industrial Aerodynamics, 2022, 229: 105160.
[10] TANG L F, LIU H J, ZHENG C R. Investigation of the wind loads and flow patterns of a high-rise building under twisted wind flows based on LES[J]. Journal of Building Engineering, 2024, 96: 110478.
[11] LIU J Y, HUI Y, YANG Q S, et al. LES evaluation of the aerodynamic characteristics of high-rise building with horizontal ribs under atmospheric boundary layer flow[J]. Journal of Building Engineering, 2023, 71: 106487.
[12] LI Z H, WANG D H, CHEN X Z, et al. Wind load effect of single-column-supported two-plate billboard structures[J]. Journal of Wind Engineering and Industrial Aerodynamics, 2018, 179: 70-79.
[13] FENG Z Q, DENG J Y, HUA X G, et al. Flutter aerodynamic shape optimization method for streamlined box girders based on support vector regression with Bayesian optimization[J]. Journal of Southeast University (Natural Science Edition), 2024, 54(2): 275-284. (in Chinese)
[14] SHEN G, HAN K, LI B, et al. Mean wind loads on T-shaped angle transmission towers[J]. Wind and Structures, 2024, 38(5): 367-379.
[15] Ministry of Housing and Urban-Rural Development of the People's Republic of China. Load code for building structures: GB 50009—2012[S]. Beijing, China: China Construction Industry Press, 2012. (in Chinese)
[16] American Society of Civil Engineers. Guidelines for electrical transmission line structural loading: ASCE NO. 74-2020[S]. Reston, VA, USA: American Society of Civil Engineers, 2020.
[17] GU M, QUAN Y. Across-wind loads and effects of super-tall buildings and structures[J]. Science China Technological Sciences, 2011, 54(10): 2531-2541.
[18] KWOK K C S. Cross-wind response of tall buildings [J]. Engineering Structures, 1982, 4(4): 256-262.
[19] LI Y, ZHANG J W, LI Q S. Experimental investigation of characteristics of torsional wind loads on rectangular tall buildings[J]. Structural Engineering and Mechanics, 2014, 49(1): 129-145.
[20] LI Y, LI Q S. Across-wind dynamic loads on L-shaped tall buildings[J]. Wind and Structures, 2016, 23(5): 385-403.
[21] HUANG S H, LI Q S, WU J R. A general inflow turbulence generator for large eddy simulation[J]. Journal of Wind Engineering and Industrial Aerodynamics, 2010, 98(10/11): 600-617.
[22] ZOU L, WU W N, WANG J H, et al. Numerical study on flow characteristics around wavy conical cylinders in triangular arrangement[J]. Journal of Southeast University (Natural Science Edition), 2024, 54(1): 224-231. (in Chinese)
[23] ZADOROZHNA D B, BENAVIDES O, GRAJEDA J S, et al. A parametric study of the effect of leading edge spherical tubercle amplitudes on the aerodynamic performance of a 2D wind turbine airfoil at low Reynolds numbers using computational fluid dynamics[J]. Energy Reports, 2021, 7: 4184-4196.
[24] ZHAO S, ZHANG X H, ZHANG C T, et al. Extreme-value combination rules for tower-line systems under non-Gaussian wind-induced vibration response[J]. Buildings, 2025, 15(11): 1871.
[25] HUANG S H, LI Q S, XU S L. Numerical evaluation of wind effects on a tall steel building by CFD[J]. Journal of Constructional Steel Research, 2007, 63(5): 612-627.

几何偏心对T形塔流场和气动力影响的大涡模拟

赵爽[1,2], 张先洪[1], 张成涛[1], 晏致涛[1,2]

(1.重庆科技大学土木与水利工程学院,重庆 401331;2.重庆市建筑科学研究院有限公司,重庆 400016)

摘要: 为研究几何偏心结构的气动性能,采用风洞试验与数值模拟方法,对不同几何偏心条件下T形塔的流场特性与气动三分力进行分析,并建立了相应的广义力谱数学模型。通过对比风洞试验与数值模拟获得的升力、阻力和扭矩系数,验证数值模拟方法的可靠性,并进一步分析了几何偏心对风压分布、涡脱特性及湍动能分布的影响。基于随机振动理论,通过对数值模拟结果的非线性拟合,得到T形塔整塔力谱的归一化公式。结果表明:偏心距越大,结构涡脱现象越复杂且向偏心侧偏移;尾流形态发生扭曲变形,呈现竖向延展特性,导致峰值风压出现在较长横臂处;扭矩系数对偏心变化的敏感度最高,偏心率增加50%时扭矩系数增加99.7%。

关键词: 几何偏心;T形塔;气动力;流场特征

中图分类号: TU312.1